Intrinsic and tunable quantum anomalous Hall effect and magnetic topological phases in XYBi$_2$Te$_5$

Xin-Yi Tang,[1] Zhe Li,[2,*] Feng Xue,[1,3] Pengfei Ji,[1] Zetao Zhang,[1]
Xiao Feng,[1,3,4] Yong Xu,[1,4,5,6] Quansheng Wu,[2,7] and Ke He[1,3,4,8]

[1] *State Key Laboratory of Low Dimensional Quantum Physics, Department of Physics, Tsinghua University, Beijing 100084, China*
[2] *Beijing National Research Center for Condensed Matter Physics, and Institute of Physics, Chinese Academy of Sciences, Beijing 100190, China*
[3] *Beijing Academy of Quantum Information Sciences, Beijing 100193, China*
[4] *Frontier Science Center for Quantum Information, Beijing 100084, China*
[5] *Tencent Quantum Laboratory, Tencent, Shenzhen, Guangdong 518057, China*
[6] *RIKEN Center for Emergent Matter Science (CEMS), Wako, Saitama 351-0198, Japan*
[7] *University of Chinese Academy of Sciences, Beijing 100049, China*
[8] *Hefei National Laboratory, Hefei 230088, China*

(Dated: July 7, 2023)

By first-principles calculations, we study the magnetic and topological properties of XYBi$_2$Te$_5$-family (X, Y = Mn, Ni, V, Eu) compounds. The strongly coupled double magnetic atom-layers can significantly enhance the magnetic ordering temperature while keeping the topologically nontrivial properties. Particularly, NiVBi$_2$Te$_5$ is found to be a magnetic Weyl semimetal in bulk and a Chern insulator in thin film with both the Curie temperature (∼150 K) and full gap well above 77 K. Ni$_2$Bi$_2$Te$_5$, MnNiBi$_2$Te$_5$, NiVBi$_2$Te$_5$ and NiEuBi$_2$Te$_5$ exhibits intrinsic dynamic axion state. Among them, MnNiBi$_2$Te$_5$ has a Néel temperature over 200 K and Ni$_2$Bi$_2$Te$_5$ even demonstrates antiferromagnetic order above room temperature. These results indicate an approach to realize high temperature quantum anomalous Hall effect and other topological quantum effects for practical applications.

I. INTRODUCTION

In the past two decades, topological states of materials have grown into a large branch of modern condensed matter physics [1–6]. Emergent topological phases, especially the ones associated with magnetism, like the quantum anomalous Hall effect (QAHE) [7–11], axion insulators (AxIs) [12–17] and magnetic Weyl semimetals (WSMs) [18–20], have attracted lots of attention. The QAHE has been experimentally achieved in Cr-doped topological insulator thin films initially in 2013 [9]. However, the reliance on extremely low temperature hindered its applications. Many candidate materials that may realize high temperature QAH insulators, magnetic WSMs or AxIs have been proposed, such as Co$_3$Sn$_2$S$_2$ [19, 20], EuIn$_2$As$_2$ [21], LiFeSe [22], PdBr$_3$-family materials [23], NiAsO$_3$ and PdSbO$_3$ [24]. Although some of them have been prepared and well-studied, quantized transport properties—the crucial mile stone—have not been achieved. Thin films of the intrinsic magnetic topological insulator MnBi$_2$Te$_4$ [25, 26] are a high temperature QAH system that has shown quantized transport properties in experiment. The magnetically induced surface state gap (briefly, magnetic gap) of MnBi$_2$Te$_4$ thin films can reach ∼50 meV [27, 28], more than enough to support QAHE above 77 K. Zero-field quantization of the anomalous Hall resistance have been observed in odd septuple-layer (SL) MnBi$_2$Te$_4$ thin flakes at 1.4 K [29], higher than that in magnetically doped (Bi,Sb)$_2$Te$_3$. Amazingly, under high magnetic field, nearly quantized Hall resistance has been observed in some MnBi$_2$Te$_4$ thin flake samples at a temperature as high as ∼40 K [30]. Other magnetic topological phases such as magnetic WSM and AxI can be realized in MnBi$_2$Te$_4$ with certain magnetic configurations and thicknesses [27, 28, 30–33]. Obviously, MnBi$_2$Te$_4$ provides a solid base for the exploration of high-temperature QAHE and other related topological quantum effects.

The temperature to achieve the QAHE is determined by both the magnetic ordering temperature and the magnetic gap size. Since the magnetic gap size of MnBi$_2$Te$_4$ thin films is as large as ∼50 meV, the bottleneck is its magnetic ordering temperature which is only ∼25 K [26]. Such a low temperature originates not only from the weak magnetic coupling strength but also from magnetic fluctuations, largely due to the two-dimensional (2D) nature of its magnetism [34]. A straightforward way to solve the two problems is to make the strongly coupled magnetic atomic layer a little thicker while not thick enough to destroy the 2D topological properties. Actually, the Curie or Néel temperature of magnetic thin films is significantly elevated as the thickness increases from monolayer to bilayer [35].

In fact, there exists such a material: Mn$_2$Bi$_2$Te$_5$, which can be considered as MnBi$_2$Te$_4$ with an additional MnTe bilayer inserted in each septuple layer (SL). The material was predicted to be a possible host of QAHE, topological magnetoelectric effect (TME) or AFM topological insu-

* lizhe21@iphy.ac.cn

lator (TI) phase depending on its layer magnetization [36–38]. $Mn_2Bi_2Te_5$ single crystals have recently been successfully prepared [39]. However, as discussed below, the inherent magnetic couplings of $Mn_2Bi_2Te_5$ are not strong and thus its magnetic ordering temperature is just 20 K. We can replace one of Mn atom layer in $Mn_2Bi_2Te_5$ with other magnetic atoms (partially discussed in Ref. [40]), or even both, namely XYBi$_2$Te$_5$ where X and Y represent magnetic atoms, to implement the above idea.

In this paper, via systematic first-principles calculations, we demonstrate our findings on high-temperature topological phases in some compounds of XYBi$_2$Te$_5$-family materials, where X, Y = Mn, Ni, V, Eu. We predict that NiVBi$_2$Te$_5$ can be a FM WSM in the bulk phase with a Curie temperature of ∼150 K and a Chern insulator in thin films that can possibily show high-temperature QAHE. Furthermore, the bulk phases of $Ni_2Bi_2Te_5$ and MnNiBi$_2$Te$_5$ are predicted to be high-temperature dynamic AxIs, in which the first one even shows magnetic ordering temperature above room temperature.

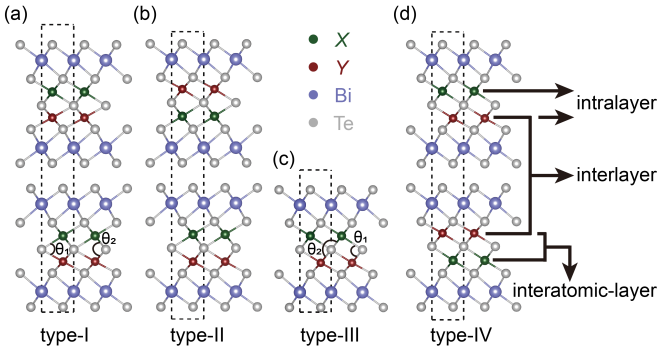

FIG. 1. Four typical structures of bulk XYBi$_2$Te$_5$. Dashed lines stands for unit cells. If X=Y, type-I and type-II (also type-III and type-IV) become the same. θ_1 and θ_2 in panels (a) and (c) are 90°-like and 180°-like angles, which are determining factors of magnetic coupling between X and Y atomic layers inside one NL. Panel (d) illustrates the three kinds of magnetic couplings discussed in Sec. III B by using type-IV lattice structure as an example.

II. METHODS

The density functional theory (DFT) calculations were carried out via the Vienna *Ab initio* Simulation Package (VASP) [41]. The projector-augmented wave (PAW) method and the plane-wave basis with an energy cutoff of 350 eV were utilized. The exchange-correlation energy is described by Perdew-Burke-Ernzerhof (PBE) functional under the generalized gradient approximation (GGA) [42]. To treat the localized d- and f-orbitals, the GGA+U approach was adopted. U parameters were selected to be 4 eV, 4 eV, 3 eV and 5 eV for Mn-3d, Ni-3d, V-3d and Eu-4f orbitals, respectively. In addition, the modified Becke-Johnson (mBJ) functional was used in bulk band computations [43]. In order to correctly describe the inherent van der Waal (vdW) interactions, the DFT-D3 method [44] was considered. Moreover, VASPKIT [45] and PHONOPY [46] codes were used for data post-processing. Plus, structural visualization was achieved with the help of VESTA [47].

The Γ-centered Monkhorst-Pack k-point meshes of 9×9×3 and 13×13×1 were adopted for bulk and thin-film structures respectively. Denser grids of 11×11×3 and 23×23×5 were used to calculate magnetocrystalline anisotropy energies (MAEs). For energy and band calculations, the geometry optimizations were performed until the Hellmann-Feynman force on each atom is smaller than 0.01 eV/Å, while the energy convergence criterion was chosen to be 1.0×10^{-6} eV. As for phonon spectra, structural relaxations were done with threshold of 1.0×10^{-4} eV/Å and 1.0×10^{-7} eV for higher accuracy and dispersion relations were calculated by density functional perturbation theory (DFPT).

The interlayer and interatomic-layer exchange energies (E_{ex}) are defined as the energy subtraction between antiferromagnetic (AFM) and ferromagnetic (FM) configurations, i.e. $E_{ex} = E_{\rm AFM} - E_{\rm FM}$. Notice that when we calculated the interlayer (interatomic-layer) E_{ex}, the interatomic-layer (interlayer) couplings were kept unchanged. The MAEs are represented by the energy subtraction between out-of-plane and in-plane configurations, i.e. $E_{\rm MAE} = E_{\text{in-plane}} - E_{\text{out-of-plane}}$. The in-plane magnetic moments are set along x-axis, since there is neglecting energy difference between x-axis and y-axis polarizations in all materials within the scope of this paper. Collinear spin-polarized calculations without spin-orbital couplings (SOCs) and non-collinear ones with SOCs were respectively conducted for the calculations of exchange energies and MAEs.

We also obtained tight-binding Hamiltonians of bulk materials based on the maximally localized Wannier functions (MLWFs) by the Wannier90 package [48–50]. Thin-film Hamiltonians were extracted from corresponding bulk ones, originated from mBJ-functional calculations. Next, all the topological properties, including Fermi surface visualizations, and Weyl points (WPs) characterizations of bulk materials, as well as edge states and Chern-number calculations of thin films, were accomplished using the tight-binding Hamiltonian method as implemented in the WannierTools package [51] based on MLWFs.

III. RESULTS

A. Lattice structures

The unit cell of XYBi$_2$Te$_5$ consists of Te-Bi-Te-X-Te-Y-Te-Bi-Te nonuple layers (NLs), with a vdW vacuum gap between neighboring NLs. There have been published theoretical works [36, 37] focusing on $Mn_2Bi_2Te_5$, one special case of XYBi$_2$Te$_5$ where X=Y=Mn. They

TABLE I. Space group of different lattice structures. Magnetic moments have been ignored. When $X=Y$, type-I and type-II (also type-III and type-IV) become the same, so we omit the space group of type-II (and type-IV) in this table.

	type-I	type-II	type-III	type-IV
$X=Y$	No. 194		No. 164	
$X\neq Y$	No. 186	No. 164	No. 156	No. 164

assumed an ABC-stacking structure of the internal Mn-Te bilayer structures, which is similar with the well-known $MnBi_2Te_4$. There are also different viewpoints on what the most stable structure should be like. As the number of Mn-Te bilayers increases, these atomic layers may tend to form an $ABAC$-stacking structure [52, 53] which resembles the bulk phase of MnTe, and this seems to be the case in $Mn_2Bi_2Te_5$-family materials [38].

Beyond MnTe, bulk phases of NiTe and VTe also appear as $ABAC$-stacking, while EuTe remains ABC-stacking [54]. This suggests that $ABAC$-stacking and ABC-stacking lattice structures (NiAs-type and NaCl-type respectively [38]) may coexist in XYBi$_2$Te$_5$ when different magnetic elements are included.

Therefore, we took both types of lattice structures into consideration. Another important question is the ordering of magnetic atomic layers when $X\neq Y$. To answer it, we studied two simple bulk models with the sequence of magnetic atomic layers being like "$\cdots$-XY-XY-XY-XY-$\cdots$" (XY-XYBT) or "$\cdots$-XY-YX-XY-YX-$\cdots$" (XY-YXBT). Thus a total of four lattice structures, named as type-I, type-II, type-III and type-IV, were investigated, as depicted in Fig. 1. These four typical structures are NiAs-type XY-XYBT (type-I), NiAs-type XY-YXBT (type-II), NaCl-type XY-XYBT (type-III) and NaCl-type XY-YXBT (type-IV). Their corresponding space group is shown in Table I. Monolayer XYBi$_2$Te$_5$, however, can just reflect the stacking order inside one single NL, so only two types of structures should be considered (type-I and type-III).

The relaxed lattice constants of both monolayer and bulk XYBi$_2$Te$_5$ (X, Y=Mn, Ni, V, Eu) compounds are demonstrated in Appendix A. To confirm the structural stability, we performed calculations on phonon dispersions. Due to the layered-stacking nature of XYBi$_2$Te$_5$, we only carried out phonon-dispersion computations on monolayers. Monolayers with type-I and type-III lattice structures can be seen as basic building blocks of all the structures discussed here. Therefore, we analyzed the twenty monolayer structures as a whole. Their phonon spectra are shown in Fig. 2. For the majority of them, no virtual frequency exists, indicating that either NiAs-type or NaCl-type XYBi$_2$Te$_5$ should be stable. The only exception appears in NaCl-type $Ni_2Bi_2Te_5$ since there is slight virtual frequency of the acoustic phonons around the Γ point [see Fig. 2(b)]. This is not a rare case in first-principles calculations and might be a result of insufficient accuracy [27, 55, 56]. For this reason, the stability of NaCl-type $Ni_2Bi_2Te_5$ may be possibly acceptable (perhaps metastable) and we still include it in the following sections also for the completeness of this work.

We also examined the influence of X-Y mixing (for $X \neq Y$ only) on structural stability. Here X-Y mixing refers to situations where the two distinguishable kinds of magnetic atoms are mixed instead of locating at separate atomic layers [see Fig. 1]. Our systematic investigation suggests that X-Y mixing will result in significant virtual frequencies on phonon spectra, which is direct evidence for structural instability. Therefore, we think it is reasonable to study XYBi$_2$Te$_5$ structures without X-Y mixing problem. Computational details can be found in Appendix B.

B. Magnetic properties

We then come to discuss the magnetic properties of XYBi$_2$Te$_5$. Both of the ground state magnetic configurations and the coupling strength are determined by superexchange rules [57]. In XYBi$_2$Te$_5$, three types of magnetic couplings determine the stable magnetic configurations, including couplings between X and Y atoms in neighboring NLs (interlayer couplings), between X or Y atoms in the same atomic layer plane (intralayer couplings), and between X and Y atoms in the same NL (interatomic-layer couplings). All of these couplings are illustrated in Fig. 1(d), where type-IV lattice structure is used as an example. The interlayer and intralayer couplings resemble those in $MnBi_2Te_4$-family materials, originated from Goodenough-Kanamori 180° and 90° rules separately [27, 31, 32, 58], so we mainly need to understand the extra interatomic-layer couplings.

Table II shows values of interlayer/interatomic-layer E_{ex}, and also MAE of XYBi$_2$Te$_5$-family materials. Similar to the $MnBi_2Te_4$-family materials, the sign and relative strength of the magnetic couplings can also be understood with the Goodenough-Kanamori rules [58]. Here, we focus on the interatomic-layer couplings which are expected to be much stronger than the interlayer ones. Firstly, we analyze the type-III structure, whose inherent ABC-stacking structure resembles that of well-known $MnBi_2Te_4$. Its interatomic-layer couplings are contributed by two kinds of hopping channels of X-Te-Y bonds, one with the bond angle near 90° [θ_1 in Fig. 1(c)], and the other with the bond angle near 180° [θ_2 in Fig. 1(c)]. The signs of the couplings contributed by the two channels (referred as θ_1 and θ_2 channels below, respectively) are opposite [see Fig. 3(a)]. θ_1 and θ_2 values of type-III XYBi$_2$Te$_5$ are summarized in Fig. 3(b). For $Ni_2Bi_2Te_5$ and $V_2Bi_2Te_5$, θ_2 is very close to 180°, meanwhile θ_1 deviates several degrees from 90°. Therefore, the coupling is dominated by the θ_2 channel which is AFM. The interatomic-layer coupling of NiVBi$_2$Te$_5$ is also dominated by the θ_2 channel, which however gives a FM ground state since the number of $3d$ electron is above five in Ni and below five in V [58]. In $Mn_2Bi_2Te_5$,

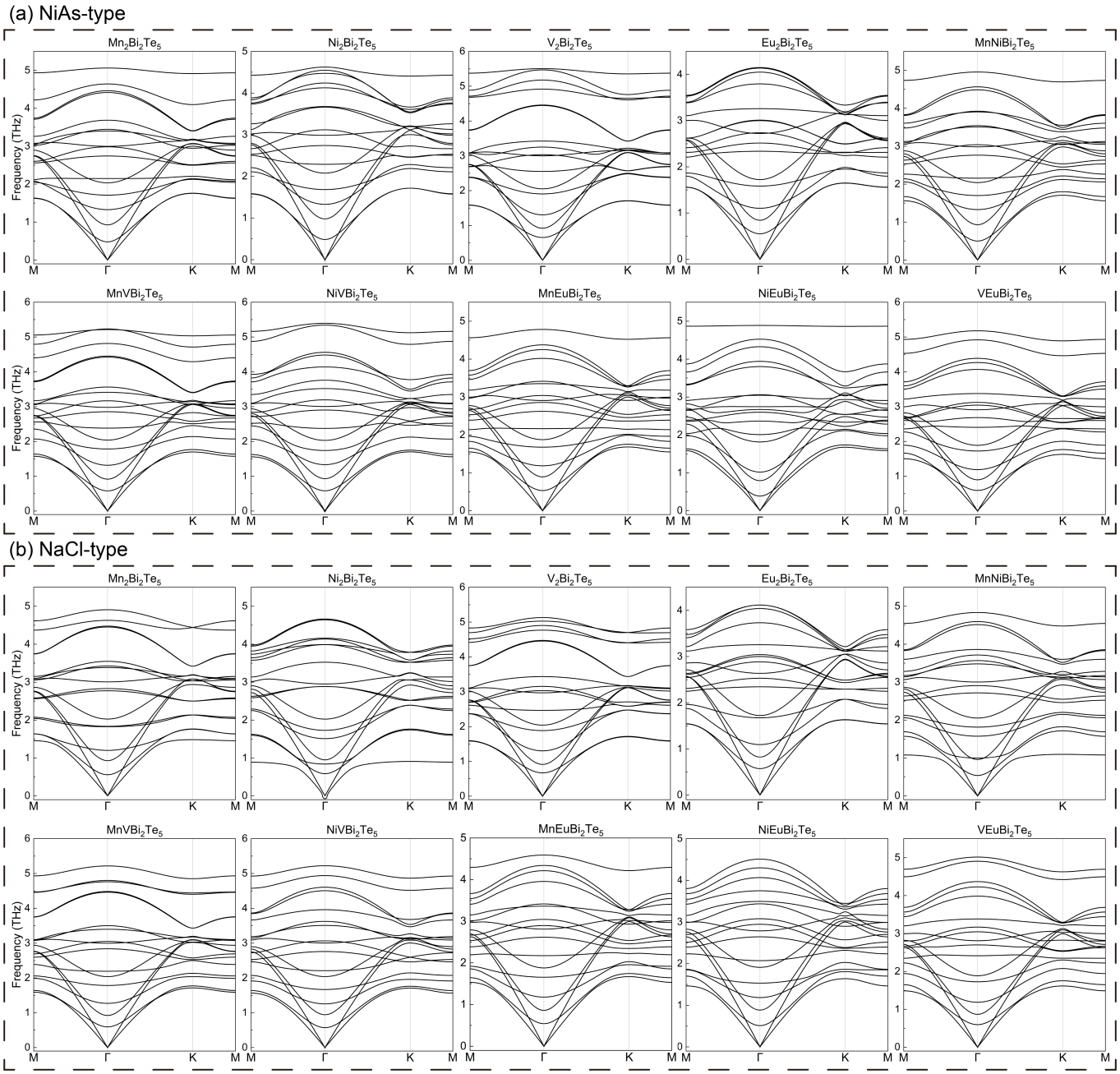

FIG. 2. Phonon dispersions of (a) type-I (NiAs-type) and (b) type-III (NaCl-type) monolayer $XY\mathrm{Bi_2Te_5}$-family materials.

the interatomic-layer coupling is even smaller than the interlayer one. It is because the couplings via the θ_1 and θ_2 channels are largely compensated with each other. Note that by varying the on-site Coulomb repulsion U or the exchange-correlation functionals [see Fig. 3(c)], the interatomic-layer coupling of $\mathrm{Mn_2Bi_2Te_5}$ can be changed from FM to A-type AFM. This does not contradict previous work on $\mathrm{Mn_2Bi_2Te_5}$ [36–38]. Nonetheless, whether the interatomic-layer coupling in $\mathrm{Mn_2Bi_2Te_5}$ is FM or AFM has not been checked by experiment [39].

The values of θ_1 in $X\mathrm{EuBi_2Te_5}$ also approach 90°, but the reverse (caused by 90°-rule) of interatomic-layer coupling ground state which is mainly determined by 180°-rule does not appear. It can be understood in the following way. According to typical superexchange mechanism, the coupling strength of the 180° rule and the 90° rule can be expressed as [57]

$$J_{180} = \frac{4t_{pd}^4}{(U_d+\Delta_{pd})^2}\left(\frac{1}{U_d}+\frac{1}{U_d+\Delta_{pd}}\right), \qquad (1)$$

$$J_{90} = -\frac{4t_{pd}^4}{(U_d+\Delta_{pd})^2}\frac{2J_{xy}}{4\left(U_d+\Delta_{pd}\right)^2-J_{xy}^2}, \qquad (2)$$

TABLE II. Summary of interlayer/interatomic-layer E_{ex} (in unit of meV) and MAE (meV/NL) of bulk XYBi$_2$Te$_5$ materials. Positive (negative) values stand for FM (AFM) coupling in E_{ex}, as well as out-of-plane (in-plane) magnetization direction in MAE.

X-Y		type-I	type-II[a]	type-III	type-IV[a]
Mn-Mn	Interlayer	-1.48		-1.74	
	Interatomic	-58.45		1.36	
	MAE	0.34		0.18	
Ni-Ni	Interlayer	-9.77		-10.82	
	Interatomic	-283.38		-266.89	
	MAE	2.59		5.22	
V-V	Interlayer	-0.56		-0.68	
	Interatomic	-156.41		-96.10	
	MAE	-0.46		-0.17	
Eu-Eu	Interlayer	-0.14		-0.11	
	Interatomic	-0.74		-3.17	
	MAE	-0.08		-0.06	
Mn-Ni	Interlayer	-3.62	-8.06	-4.14	-8.23
	Interatomic	-132.65	-135.32	-104.69	-106.89
	MAE	1.90	1.33	2.18	2.53
Mn-V	Interlayer	1.66	-1.44	1.33	-0.85
	Interatomic	-33.07	-32.42	34.40	34.90
	MAE	-0.14	-0.13	-0.03	-0.07
Ni-V	Interlayer	1.41	-11.55	1.59	-8.89
	Interatomic	56.69	58.10	84.46	85.25
	MAE	0.94	1.08	0.85	1.00
Mn-Eu	Interlayer	0.25	-0.57	0.38	-0.56
	Interatomic	15.25	15.38	11.68	11.38
	MAE	0.05	0.06	0.10	0.11
Ni-Eu	Interlayer	0.27	-9.19	0.80	-12.48
	Interatomic	28.24	26.81	24.52	23.76
	MAE	0.82	0.96	1.02	1.21
V-Eu	Interlayer	-0.32	-0.44	-0.30	-0.52
	Interatomic	-1.01	-2.91	-13.43	-13.71
	MAE	-0.13	-0.11	-0.09	-0.06

[a] In Type-II and Type-IV structures, two kinds of interlayer couplings exist because of the XY-YX order. Hence, the interlayer E_{ex} here can be seen as the average values of them.

$$J_{90}/J_{180} \approx -\frac{-U_d J_{xy}}{2\left(U_d+\Delta_{pd}\right)\left(2U_d+\Delta_{pd}\right)}. \qquad (3)$$

Here t_{pd} represents hopping strength between p and d orbitals. U_d stands for Hubbard U term of magnetic atoms, while Δ_{pd} can be obtained by subtracting the energy of occupied p orbitals from that of occupied d orbitals. J_{xy} is the Coulomb exchange term between two orthogonal p orbitals. Eq. (3) is extracted by considering $J_{xy} \ll U_d+\Delta_{pd}$. The $5d$ orbitals of Eu, compared with $3d$ orbitals of Mn, V and Ni, locate quite far away from the Fermi level [58]. So, Δ_{pd} of materials containing Eu is obviously larger than that of others, leading to weaker contributions from 90° rule. Therefore, there is no anomaly in the interatomic-layer couplings of XEuBi$_2$Te$_5$.

The above analysis on type-III structure is also suitable for type-IV, since they bare resembling X-Te-Y bond structures and also interatomic-layer E_{ex}. However, due to the $ABAC$-stacking order in type-I and type-II structures, the θ_1 and θ_2 stay far away from either 180° or 90° [see Fig. 1(a)] and it becomes hard to qualitatively settle the interatomic-layer couplings via Goodenough-Kanamori 180° and 90° rules. Also, the shortest distance between magnetic atoms in the two separate layers becomes smaller in NiAs-type structure ($\lesssim$4 Å) than that in NaCl-type structure and even the distance between the nearest magnetic atoms within one atomic layer (>4 Å), which means the direct exchange interaction should not be ignored, making the interatomic-layer couplings more complicated. Based on DFT calculations, we found that, besides Mn$_2$Bi$_2$Te$_5$ mentioned in Ref. [38], the interatomic-layer coupling of MnVBi$_2$Te$_5$ also changes (both from FM to AFM) when the lattice structures evolve from NaCl-Type to NiAs-type, while others remain unchanged.

After figuring out the magnetic couplings and especially the ground state configurations of all XYBi$_2$Te$_5$, we tried to make it clear which of the four lattice structures proposed in this paper, should be energetically the most favorable. As can be seen in Fig. 4, we made comparisons of ground state energies within every kind of XYBi$_2$Te$_5$. A NiAs-type lattice structure is preferred when Eu is excluded from the component magnetic elements, while a NaCl-type lattice structure is preferred once Eu is included. This may be a result of the lackness of $ABAC$-stacking structure in bulk phase EuTe, as mentioned before. With the increasing number of magnetic-cation and Te-anion bilayers, the local chemical environment around magnetic atoms will approach that in their corresponding bulk phases, leading to similar stacking orders eventually.

Another finding is about the sequence of magnetic atomic layers. It is influenced by the strength of interlayer couplings. For example, the energetically favorite structures in MnNiBi$_2$Te$_5$ (type-II), NiVBi$_2$Te$_5$ (type-II) and NiEuBi$_2$Te$_5$ (type-IV) are all XY-YXBT. This is because the interlayer coupling between Ni atomic layers is much stronger than others [see Table II], which is beneficial for lowering the total energy. This rule is not apparent or applicable to cases where the strength of interlayer couplings between X-X, Y-Y and X-Y are comparable, since their relative values may be sensitive to even slight change in lattice structures. MnVBi$_2$Te$_5$ and MnEuBi$_2$Te$_5$ are two typical examples. Negligible energy difference is found between their type-I(III) and type-II(IV) structures.

We estimated the Néel/Curie temperatures of selected bulk XYBi$_2$Te$_5$ materials with Monte Carlo (MC) simulations, mainly including the six XYBi$_2$Te$_5$ with out-of-plane magnetic ground states [see Table II]. A Heisenberg model was employed to describe their magnetic behaviors, which involves the aforementioned three kinds of magnetic couplings up to next-nearest neighbors and single-ion anisotropy energy.

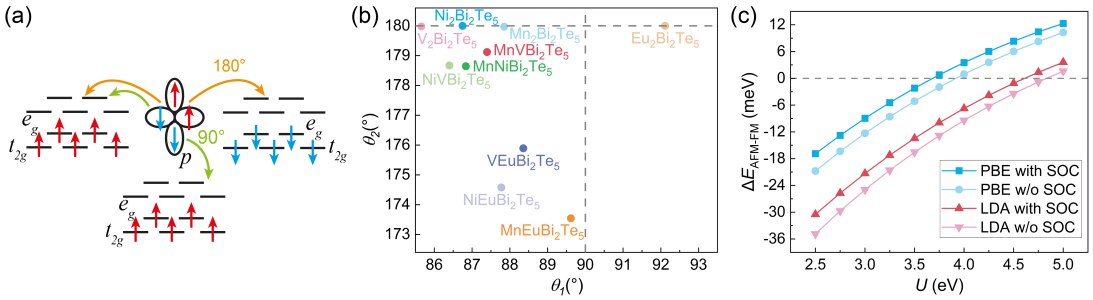

FIG. 3. Interatomic-layer couplings of type-III XYBi$_2$Te$_5$. (a) Schematic illustration of the Goodenough-Kanamori 180° and 90° superexchange mechanisms. Here we adopt d orbitals of Mn as an example. (b) Bond angle values of type-III XYBi$_2$Te$_5$. (c) Energy difference between FM and AFM interatomic-layer couplings of type-III Mn$_2$Bi$_2$Te$_5$ obtained with different U and exchange-correlation functionals.

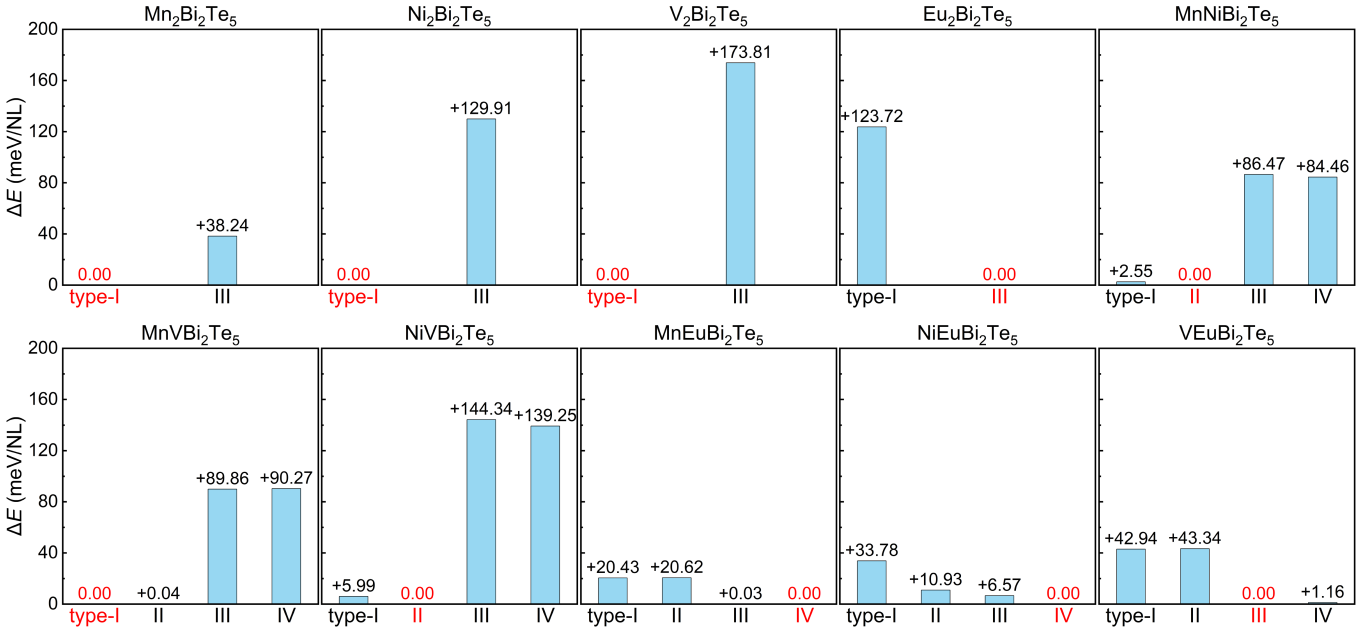

FIG. 4. Energy comparisons of magnetic ground states based on four types of bulk phase XYBi$_2$Te$_5$ lattice structures (two types indeed when $X=Y$). The lowest energies are equally set to zero and marked in red in every compound of XYBi$_2$Te$_5$. Type-II MnVBi$_2$Te$_5$ and type-III MnEuBi$_2$Te$_5$ may be quasi-ground states since they show slight difference compared to type-I MnVBi$_2$Te$_5$ and type-IV MnEuBi$_2$Te$_5$ respectively, which is beyond the precision of computations.

$$H = \sum_{i\in X,Y} A_i (S_i^z)^2 + \sum_{i,j\in X} J_{ij}^X \boldsymbol{S}_i \cdot \boldsymbol{S}_j + \sum_{i,j\in Y} J_{ij}^Y \boldsymbol{S}_i \cdot \boldsymbol{S}_j + \sum_{i,j\in \text{interlayer}} J_{ij}^I \boldsymbol{S}_i \cdot \boldsymbol{S}_j + \sum_{i,j\in \text{interatomic-layer}} J_{ij}^S \boldsymbol{S}_i \cdot \boldsymbol{S}_j. \quad (4)$$

A_i, J_{ij}^X and J_{ij}^Y are single ion anisotropy energy and the intralayer couplings in X and Y atomic layers respectively. J_{ij}^I and J_{ij}^S refer to interlayer and interatomic-layer interaction parameters. Note that in type-II and type-IV structures, J_{ij}^I can be further decomposed into J_{ij}^{IX} and J_{ij}^{IY} in order to describe the two kinds of interlayer couplings.

During simulations, we firstly adopted 2×10^5 MC steps for equilibrating the system at each temperature, and next 1×10^6 steps for computing physical quantity such as heat capacity. A supercell of $12\times12\times3$ unit cells as well as periodic boundary conditions were used. Larger supercell were also tested, and we find in general a supercell of $12\times12\times3$ is enough.

As shown in Fig. 5, type-I Ni$_2$Bi$_2$Te$_5$, type-II NiVBi$_2$Te$_5$ and type-II MnNiBi$_2$Te$_5$ have Néel/Curie temperatures above 77 K, in which type-I Ni$_2$Bi$_2$Te$_5$ even has a Néel temperature above room temperature. The result coincides with their strong interatomic-layer couplings (all above 50 meV per unit cell) shown in Tab. II.

Our calculation for type-I Mn$_2$Bi$_2$Te$_5$ shows a moderate value of its Néel temperature (61 K), which is much

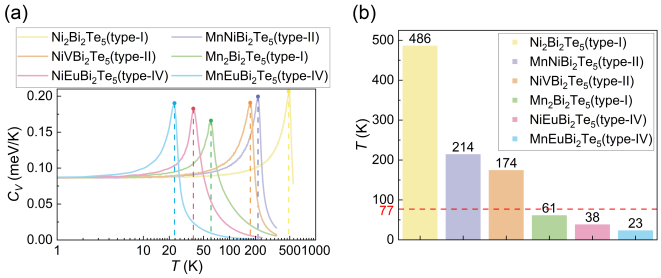

FIG. 5. Néel/Curie temperatures of six kinds of $XY\mathrm{Bi_2Te_5}$ materials with out-of-plane magnetic ground states. (a) C_V-T curves of those $XY\mathrm{Bi_2Te_5}$ combinations obtained by Monte Carlo simulations. (b) Their corresponding Néel/Curie temperatures are extracted and shown in a bar chart for clarity. The boiling temperature of liquid nitrogen (77 K) is marked with a red dashed line.

higher than what was obtained in experiment [39] and another theoretical work [38]. However, it's worth mentioning that our calculations for type-III $\mathrm{Mn_2Bi_2Te_5}$ (27 K) is close to the experimental result (20 K) [39] (see Appendix C). This might imply that the $\mathrm{Mn_2Bi_2Te_5}$ samples synthesized in laboratories possessed a stable but not energetically favorite structure (type-III, not type-I), which is also likely to happen in other $XY\mathrm{Bi_2Te_5}$ combinations. We think more experimental information, like images of atomically resolved high-angle annular dark field STEM, is necessary before the end of this structural puzzle.

One can see from Fig. 5 and Tab. II that the compounds including Ni atoms have higher Néel/Curie temperature. The projected band structures and partial density of states (DOS) of Ni, V, Mn and Eu are plotted in Fig. 6 respectively. Appreciably, the distributions of Ni $3d$ orbitals locate near the Fermi level, which benefit the virtual hopping processes and greatly enhance the magnetic coupling strength [57]. With unoccupied e_g orbitals situating even nearer the Fermi level, Ni behaves much better than V. In contrast, the Mn $3d$ and Eu $5d$ orbitals locate quite far from the Fermi level, generating much weaker coupling strength.

C. Band topologies

Now we are ready to talk about both the intrinsic and tunable magnetic topological properties of $XY\mathrm{Bi_2Te_5}$-family materials. Up to now, experimental results [39] are not sufficient to decide which type of lattice structures can be achieved in laboratory. Besides, due to the quite weak vdW interactions, it may be possible to artificially tune the interlayer stacking orders of X and Y atomic layers by methods like exfoliation. Therefore, although it is theoretically reasonable to exclusively discuss the structures with the lowest energies, we extend our discussions beyond this range and consider other dynamically stable lattice structures if necessary.

Firstly, we discuss about a kind of symmetry-protected

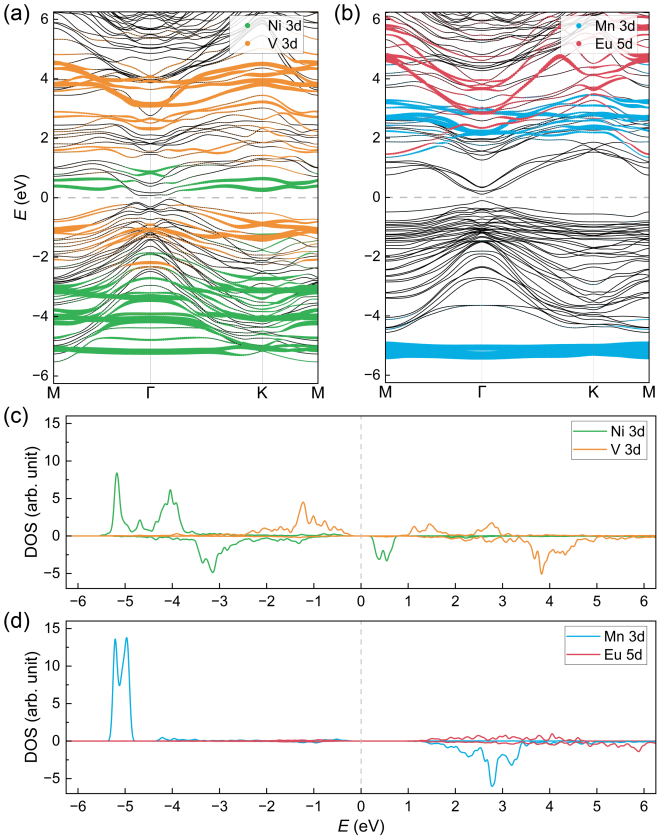

FIG. 6. Band structures along high symmetry lines (with SOC) and partial DOS distributions (without SOC) using monolayer type-I $\mathrm{NiVBi_2Te_5}$ (a, c) and type-III $\mathrm{MnEuBi_2Te_5}$ (b, d) as examples. We have highlighted the d-orbital components related to magnetic couplings.

topological phase. It was reported that in a system whose low-energy physics can be described by a $\mathrm{Bi_2Te_3}$-like effective Hamiltonian [59, 60], a $\mathcal{P}$-breaking, $\mathcal{T}$-breaking and $\mathcal{PT}$-conserving perturbation brings chances on achieving dynamic axion states [13]. This has been theoretically shown in type-III $\mathrm{Mn_2Bi_2Te_5}$ with A-type AFM magnetic configuration [36, 37].

Beyond this, we also found intrinsic dynamic axion states in type-I $\mathrm{Ni_2Bi_2Te_5}$, type-II $\mathrm{MnNiBi_2Te_5}$, type-II $\mathrm{NiVBi_2Te_5}$ and type-IV $\mathrm{NiEuBi_2Te_5}$, but not in type-I $\mathrm{Mn_2Bi_2Te_5}$ by mBJ+U calculations. They are all stable and energetically favored lattice structures. Besides, their ground state magnetic couplings [see Table II and Fig. 4], together with the lattice structures, satisfied the aforementioned symmetry constraints. Although they belong to different space groups from $\mathrm{Bi_2Te_3}$ (No. 166), the threefold rotation along the c direction, twofold rotation along the a direction and also inversion symmetry (when magnetic moments are ignored) remain, which means a perturbed $\mathrm{Bi_2Te_3}$-like effective Hamiltonian is still applicable.

As reported previously, a band inversion process without gap-closing point and gapped surface states on all

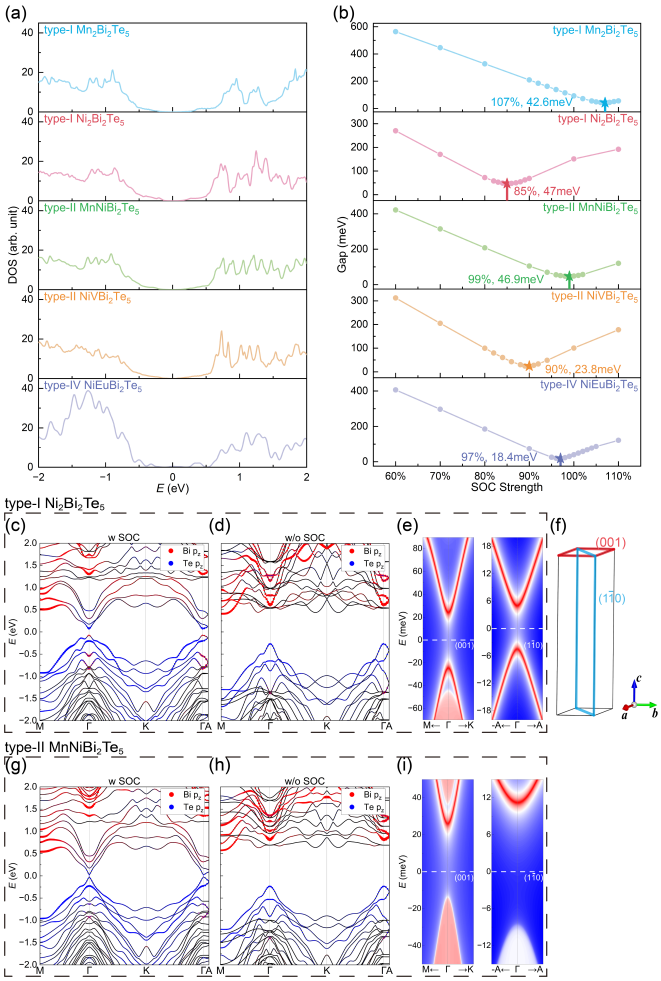

FIG. 7. Intrinsic dynamic axion states in ground state $XY\mathrm{Bi_2Te_5}$. (a) DOS of the five candidates. SOC is considered. (b) The evolution of band gap under increasing SOC strength. (c, d) Band structures of type-I $\mathrm{Ni_2Bi_2Te_5}$ with SOC (w SOC) and without SOC (w/o SOC), respectively. (e) Calculated surface states of type-I $\mathrm{Ni_2Bi_2Te_5}$ on its (001) and $(1\bar{1}0)$ planes. (f) Schematic illustration of these two surfaces. Panels (g) to (i) are similar with panels (c) to (e), but demonstrate situations in type-II $\mathrm{MnNiBi_2Te_5}$.

surfaces are supposed to appear in materials preserving $\mathcal{PT}$ symmetry but breaking individual $\mathcal{P}$ and $\mathcal{T}$ symmetries, serving as the signatures on the emergence of dynamic axion fields [61]. Figure 7(a) clearly illustrates the insulating behavior of type-I $\mathrm{Mn_2Bi_2Te_5}$, type-I $\mathrm{Ni_2Bi_2Te_5}$, type-II $\mathrm{MnNiBi_2Te_5}$, type-II $\mathrm{NiVBi_2Te_5}$ and type-IV $\mathrm{NiEuBi_2Te_5}$. Ground state magnetic configurations and SOC are considered. Then we artificially tuned the SOC strength and studied their band gap evolution [see Fig. 7(b)]. By increasing the SOC strength from 60% to 100%, in which 100% represents the realistic value, the band gaps in four of them firstly decreases, reaching their minimum and then reincreases. The turning point of type-II $\mathrm{MnNiBi_2Te_5}$ (99%) and type-IV $\mathrm{NiEuBi_2Te_5}$ (97%) is very close to the realistic value, thus implying large inherent dynamic axion field. However, type-I $\mathrm{Mn_2Bi_2Te_5}$ can only demonstrate this topological phase transition under a bit larger SOC strength (107%), so we claim it to be trivial.

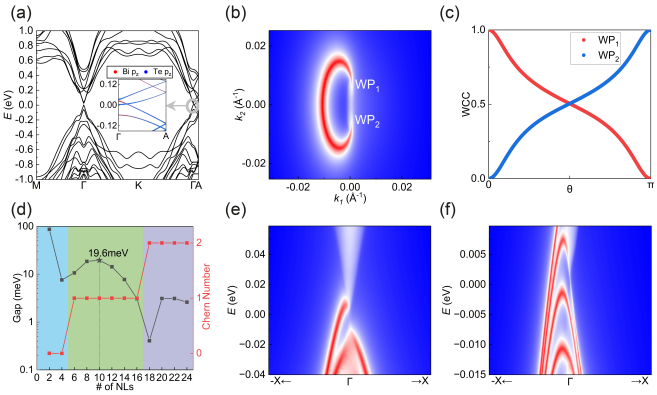

FIG. 8. Topological features of type-I $\mathrm{NiVBi_2Te_5}$ in bulk and thin films. (a) Band structure of WSM type-I $\mathrm{NiVBi_2Te_5}$. Details of projected band near one of the WPs are shown in the inset. (b) Surface states on the (100) plane, showing a Fermi arc connecting the two WPs. (c) The motions of the sum of WCCs on spheres surrounding each WP in the momentum space. (d) The evolution of band gap and Chern number with thickness of type-I $\mathrm{NiVBi_2Te_5}$ slab. Chiral edge states of (e) 6-NL ($\mathcal{C}=1$) and (f) 20-NL ($\mathcal{C}=2$) slabs.

Figures 7(c) and 7(d) show the orbital-projected band structures of type-I $\mathrm{Ni_2Bi_2Te_5}$ with and without SOC, respectively. Band inversion between Bi $6p_z$ and Te $5p_z$ indicates its topologically non-trivial character. Surface states on the (001) and $(1\bar{1}0)$ planes were calculated and the minimum gap of surface states reaches approximately 6 meV (∼74 K) [see Figs. 7(e) and 7(f)]. Figures 7(g), 7(h) and 7(i) shows the dynamic AxI features in type-II $\mathrm{MnNiBi_2Te_5}$. Specially, the minimum gap of surface states in type-II $\mathrm{MnNiBi_2Te_5}$ is larger than 17 meV (∼210 K), which is comparable with its high enough Néel temperature (∼214 K). The band inversion characters and surface state visualizations of the rest two candidates can be found in Appendix D.

In addition, we identified intrinsic magnetic topological phases beyond the aforementioned dynamic AxIs. Figure 8 shows the topological properties of type-I $\mathrm{NiVBi_2Te_5}$, a $XY\mathrm{Bi_2Te_5}$ compound with FM ground state and a high Curie temperature of ∼152 K [see Appendix C]. The band structure is demonstrated in Fig. 8(a), and one pair of Weyl points (WPs) emerge along the -$A-\Gamma-A$ line, with one of them shown in the inset. Our surface state calculations confirm that one pair of WPs exist due to $\mathcal{T}$-symmetry breaking. Figure 8(b) clearly shows that a Fermi arc connects two WPs that are symmetrically located along the -$A-\Gamma-A$ on the (100) surface plane. Two WPs demonstrate opposite chirality by checking the motions of the sum of Wannier charge centers (WCCs) [see Fig. 8(c)], indicating that type-I $\mathrm{NiVBi_2Te_5}$ exhibits a intrinsic WSM state in bulk under zero external magnetic

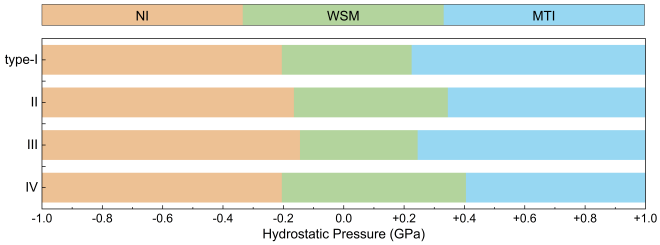

FIG. 9. Phase diagrams of out-of-plane FM $NiVBi_2Te_5$ obtained by tuning external pressures. The orange, green and blue zones stand for NI, WSM and MTI phase, respectively.

field. The strong magnetic coupling makes $NiVBi_2Te_5$ a charming magnetic WSM with high enough Curie temperature (up to 152 K). Beyond type-I $NiVBi_2Te_5$, intrinsic high-temperature WSM phase can also appear in type-III $NiVBi_2Te_5$. See Appendix E for more discussions.

The intrinsic bulk WSM phase in type-I (also type-III) $NiVBi_2Te_5$ indicates that its thin films can host Chern insulator phases with Chern number growing with increasing thickness [62]. Figure. 8(d) shows the evolution of the gap size and the Chern number with thickness, which were calculated using maximally localized Wannier function (MLWF) based tight-binding models. A type-I $NiVBi_2Te_5$ film is a normal insulator below 6-NL, Chern insulator with $\mathcal{C} = 1$ between 6-NL and 16-NL, and high Chern insulator ($\mathcal{C} \geqslant 2$) above 16-NL. The relatively short distance between the two WPs leads to slow growth of Chern number, compared to that of FM state $MnBi_2Te_4$ [30]. Naturally, the slab band gaps experience a close and reopen process every time the Chern number changes. In the Chern insulator region, which supports QAHE, the full gap reaches its maximum value of 19.6 meV in 10-NL slabs, corresponding to 227 K. Figures 8(e) and 8(f) demonstrate the calculated chiral edge states of 6-NL and 20-NL respectively, validating the Chern insulator phases with Chern number $\mathcal{C} = 1$ and $\mathcal{C} = 2$ respectively.

In order to further understand the origin of WSM in bulk phase $NiVBi_2Te_5$, and also the tunability of different topological phases, we investigated the topological properties of $NiVBi_2Te_5$ under hydrostatic pressures from -1.0 GPa to +1.0 GPa, where ambient pressure is labeled as 0.0 GPa and experimentally unavailable negative pressure conditions were adopted to complete the study of phase transition. We studied the electronic structures of bulk $NiVBi_2Te_5$ with out-of-plane FM magnetization. This magnetic configuration is exactly the magnetic ground state of type-I and type-III $NiVBi_2Te_5$. It can also be achieved in type-II and type-IV $NiVBi_2Te_5$ if their AFM interlayer couplings are flipped under strong enough external magnetic field.

Three topologically distinguishable types of pressure-induced topological phases are identified in Fig. 9, including normal insulator (NI), WSM and magnetic topological insulator (MTI). Different phases of bulk $NiVBi_2Te_5$ corresponds to different 2D phases in thin films. As the thin films grow thicker, the Chern number of NIs fixes at zero and that of WSMs grows as analyzed in Fig. 8(d), while that of MTI jumps from zero to one at certain thickness and remains unchanged afterwards. In the pressure range discussed here, all types of $NiVBi_2Te_5$ behaves like NI at low pressure, evolves into WSM near the ambient pressure region and steps into MTI eventually at high pressure.

Theoretically there have been well-established phase diagrams of NI-WSM(QAH)-MTI transition based on magnetically doped NI-TI superlattices [63, 64]. In these models, intralayer coupling strength Δ_S between top and bottom surface states (SSs), interlayer coupling strength Δ_D between bottom and top SSs of neighboring layers, and Zeeman splitting denoted as m decide the final topological character. Increasing (Decreasing) the external pressure can shrink (enlarge) the ratio between Δ_S and Δ_D, leading to phase transitions. Besides, symmetries play a crucial rule, and the basic model in Ref. [63] requires the presence of inversion symmetry $\mathcal{P}$. Once $\mathcal{P}$ is broken, two extra parameters including the electrostatic potential difference V between bottom and top SSs, and Dresselhaus-like SOC interaction λ, should be considered to handle the symmetry change [64].

For $NiVBi_2Te_5$, $\mathcal{P}$ is conserved in type-II and type-IV structures, while broken in type-I and type-III structures. However, Ni and V atoms share very similar size and thus SOC strength, leading to ignorable λ. Based on Ref. [64], the phase diagram remains almost unchanged as long as we replace m with an effective Zeeman splitting parameter $\sqrt{m^2 - V^2}$. Therefore, it's reasonable that all these four compounds can experience a phase transition from NI to WSM and MTI under different external pressure.

IV. CONCLUSIONS

In conclusion, we systematically study the structural, magnetic and topological properties of $XYBi_2Te_5$-family materials. Interatomic-layer exchange couplings play a crucial role in keeping magnetic order of some compounds above 77 K (several compounds even above 150 K), while interlayer couplings and hybridization between top and bottom surfaces determine the band topology. We find type-I(III) $NiVBi_2Te_5$ to be an emergent material with high Chern number and possible high-temperature ($\sim$152 K) QAHE state and type-I $Ni_2Bi_2Te_5$ as another candidate demonstrating above-room-temperature AFM order. $Ni_2Bi_2Te_5$, as well as some other kinds of $XYBi_2Te_5$ like type-II $MnNiBi_2Te_5$, type-II $NiVBi_2Te_5$ and type-IV $NiEuBi_2Te_5$, also demonstrates nontrivial dynamic axion states. The surface state gaps of, for example, type-II $MnNiBi_2Te_5$ ($\sim$17 meV) can be large enough for high-temperature explorations. Under external pressure or magnetic field, possible high-temperature WSM and QAH phases can also be tunable.

ACKNOWLEDGMENTS

We thank Boxuan Li for helpful discussions and Jiaheng Li for technical support. This work was supported by the National Natural Science Foundation of China (92065206).

X.-Y.T. and Z.L. contributed equally to this work.

Appendix A: LATTICE CONSTANTS OF MONOLAYER AND BULK XYBi$_2$Te$_5$

The lattice constants are almost the same under different magnetic configurations. Thus we only demonstrate the data calculated at magnetic ground states. Detailed discussions on intrinsic magnetism of XYBi$_2$Te$_5$ can be found in Sec. III B. For Mn$_2$Bi$_2$Te$_5$, all presented data in this paper are based on theoretical lattice constants. The difference between theoretical and reported experimental lattice constants [39] of bulk Mn$_2$Bi$_2$Te$_5$ is less than 1%.

TABLE III. Lattice constants of all ten kinds of XYBi$_2$Te$_5$ combinations. Here a and c refer to in-plane and out-of-plane lattice constants individually. Both are in unit of Å.

	X-Y		type-I	type-II	type-III	type-IV
Mn-Mn	monolayer	a	4.338		4.333	
	bulk	a	4.310		4.307	
		c	33.951		17.045	
Ni-Ni	monolayer	a	4.222		4.189	
	bulk	a	4.289		4.243	
		c	32.393		16.423	
V-V	monolayer	a	4.337		4.325	
	bulk	a	4.315		4.307	
		c	33.377		16.819	
Eu-Eu	monolayer	a	4.537		4.549	
	bulk	a	4.519		4.532	
		c	35.864		17.734	
Mn-Ni	monolayer	a	4.276		4.257	
	bulk	a	4.285	4.285	4.261	4.259
		c	33.196	33.256	16.718	33.452
Mn-V	monolayer	a	4.336		4.323	
	bulk	a	4.311	4.311	4.301	4.302
		c	33.771	33.786	16.994	33.994
Ni-V	monolayer	a	4.283		4.258	
	bulk	a	4.263	4.262	4.265	4.266
		c	32.925	33.113	16.697	33.393
Mn-Eu	monolayer	a	4.405		4.438	
	bulk	a	4.400	4.405	4.419	4.420
		c	35.049	35.071	17.404	34.830
Ni-Eu	monolayer	a	4.363		4.362	
	bulk	a	4.333	4.347	4.355	4.356
		c	34.646	34.602	17.175	34.340
V-Eu	monolayer	a	4.499		4.427	
	bulk	a	4.398	4.398	4.409	4.355
		c	34.938	34.907	17.326	34.472

Appendix B: DISCUSSIONS ON XYBi$_2$Te$_5$ WITH X-Y MIXING

We considered the situations where X and Y atoms ($X \neq Y$) are mixed instead of locating at separate atomic layers. We showed that for some combinations of X and Y, X-Y mixing is neither energetically favored nor structurally stable. For the others, despite X-Y mixing leads to energy gain, the structural instability remains.

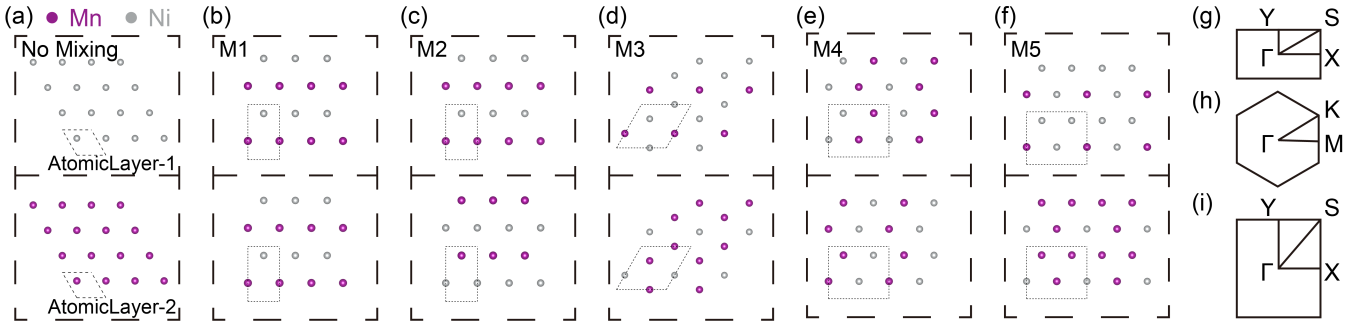

FIG. 10. Illustration of X-Y mixing using monolayer type-I $MnNiBi_2Te_5$ as an example. (a) Pristine lattice structure with only Ni (AtomicLayer-1) and Mn (AtomicLayer-2) atomic layers plotted. (b-f) Five considered lattice structures with X-Y mixing are denoted as M1-M5. Only the two magnetic atomic layers are plotted for clarity. We marked the unit cells inside every layer as thin dashed lines. (g-i) Schematic first Brillouin zones of M1-M2, M3 and M4-M5.

Taking monolayer XYBi$_2$Te$_5$ as an example, we constructed five representative structures with X-Y mixing, denoted as M1-M5 [see Figs. 10(b-f)]. Each magnetic atomic layer in M1(M2) shows stripy structures. The only difference between M1 and M2 is the interatomic-layer stacking order. M3 simulates the mixing problem using a $\sqrt{3} \times \sqrt{3}$ supercell. M4 possesses a zigzag structure while M5 is derived from M4 but with a different mixing ratio of 3:1 in each single layer. Note that the mixed structures are all based on monolayer ground-state lattice structures, which means we selected type-I $MnNiBi_2Te_5$, $MnVBi_2Te_5$ and $NiVBi_2Te_5$ but type-III $MnEuBi_2Te_5$, $NiEuBi_2Te_5$ and $VEuBi_2Te_5$ instead.

TABLE IV. Energy comparisons between mixed (M1-M5) and pristine structures of monolayer XYBi$_2$Te$_5$ ($X \neq Y$). The ground state energies of pristine structures (without mixing) are set as zero points and all values are in unit of meV. Negative (positive) values refer to occasions where mixing leads to energy gain (cost). All these values have been averaged to cells as large as original primitive cells (including one X and one Y) for better comparison.

X-Y	M1	M2	M3	M4	M5
Mn-Ni	55.08	60.07	64.47	60.68	48.71
Mn-V	-5.01	-18.57	-9.46	-11.19	-5.98
Ni-V	-71.15	-73.78	-59.87	-68.99	-52.66
Mn-Eu	134.80	4.89	64.08	74.12	37.05
Ni-Eu	114.92	82.43	109.42	55.33	102.38
V-Eu	230.44	27.26	111.52	147.97	78.15

We calculated the magnetic ground state energies of different mixed structures. Similar to calculations in Sec. III B, we also used collinear calculations and ignored SOC. The data are summarized in Table IV. As we can see, the ground state energy may be further reduced in $MnVBi_2Te_5$ and $NiVBi_2Te_5$ once Mn(Ni) and V atoms are mixed, while in other XYBi$_2$Te$_5$ considered here, separate X and Y atomic layers are energetically favored.

Then we studied the phonon dispersions of mixed structures [see Fig. 11]. We found that no matter how the X and Y atoms are mixed, significant virtual frequency across the first Brillouin zone (FBZ) emerges, indicating highly unstable structures. Specifically, the appearance of virtual frequency is not sensitive to the interatomic-layer stacking order, but highly related to the in-plane direction along which mixing happens [see M1 and M2 in Fig. 11]. The latter conclusion can be made when the phonon dispersions along $\Gamma - X$ and $\Gamma - Y$ are compared with each other in cases of M1 and M2. Therefore, we think X-Y mixing should not be a severe problem theoretically and XYBi$_2$Te$_5$ materials are supposed to inherently establish separate magnetic atomic layers.

Appendix C: SUPPLEMENTARY C_V-T CURVES of $Mn_2Bi_2Te_5$ and $NiVBi_2Te_5$

Extra C_V-T curves of $Mn_2Bi_2Te_5$ and $NiVBi_2Te_5$ are demonstrated in Fig. 12. The Curie temperatures of type-I and type-III $NiVBi_2Te_5$ (152 K and 134 K respectively) are also well above 77 K, firmly supporting the description of high-temperature WSM in the main text. We also tested the influence of SOC on the results using type-III $NiVBi_2Te_5$, type-I and type-III $Mn_2Bi_2Te_5$ as examples. Typically, the introduction of SOC leads to a slight increase in magnetic critical temperature. As for type-III $Mn_2Bi_2Te_5$, since the estimated Néel temperature is not high and close to experimental results, we decided to consider an extra next-next-nearest intralayer coupling term in our simulation and adopted experimental lattice in the calculation of exchange constants. As can be seen in Fig 12(a), its weak interatomic-layer E_{ex} leads to a Néel temperature of 10 K when SOC is ignored, while 27 K when SOC is considered, which is much closer to the experimental result than type-I $Mn_2Bi_2Te_5$.

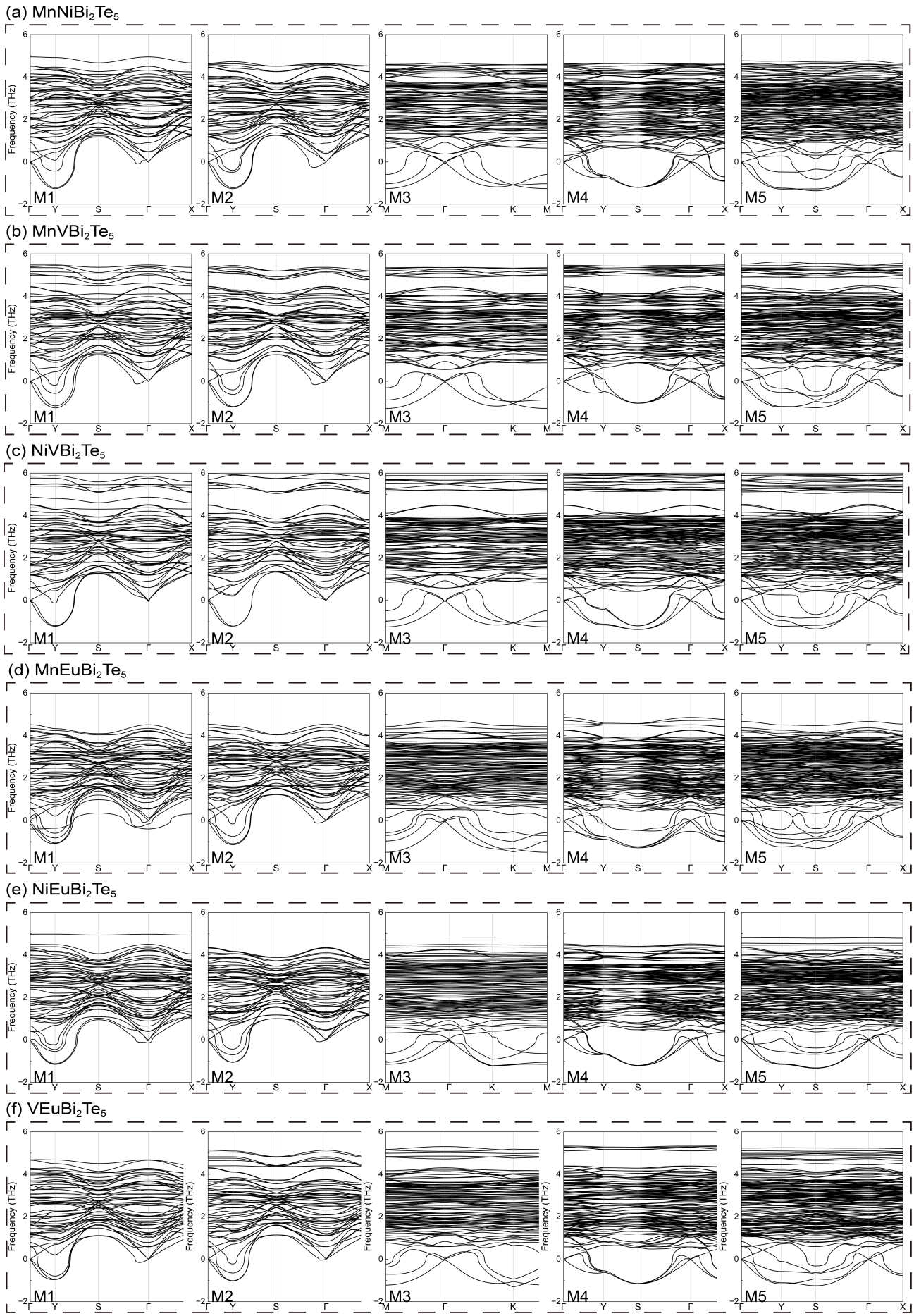

FIG. 11. Phonon dispersions of lattice structures with X-Y mixing.

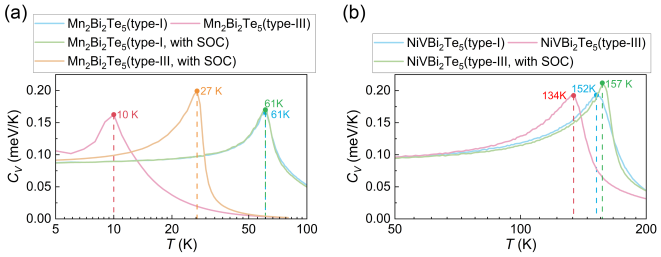

FIG. 12. C_V-T curves of (a) type-I and type-III $Mn_2Bi_2Te_5$ and (b) type-I and type-III $NiVBi_2Te_5$.

Appendix D: BAND INVERSION FEATURES AND SURFACE STATES OF DYNAMIC AXION INSULATORS

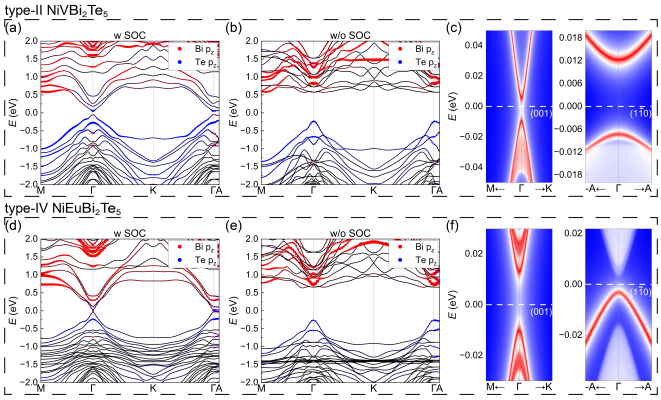

FIG. 13. Band structures and surface states of (a-c) type-II $NiVBi_2Te_5$ and (d-f) type-IV $NiEuBi_2Te_5$. (a,d) Band structures with SOC. (b,e) Band structures without SOC. (c,f) Surface states on (001) and $(1\bar{1}0)$ planes.

The bulk band structures and also surface states of type-II $NiVBi_2Te_5$ and type-IV $NiEuBi_2Te_5$ are shown in Fig. 13. Clearly, the band inversion features and gapped surface states can be found out. Combining these characters with information provided in Fig. 7, we can conclude that these two kinds of $XYBi_2Te_5$ are also dynamic AxIs.

Appendix E: WEYL SEMIMETAL AND CHERN INSULATOR PHASES OF TYPE-III $NiVBi_2Te_5$

Similar to type-I $NiVBi_2Te_5$, type-III $NiVBi_2Te_5$ also has a FM ground state and behaves as intrinsic magnetic WSM. Figure 14 summarizes the overall topological properties of type-III $NiVBi_2Te_5$ both in its 3D bulk phase and 2D thin films.

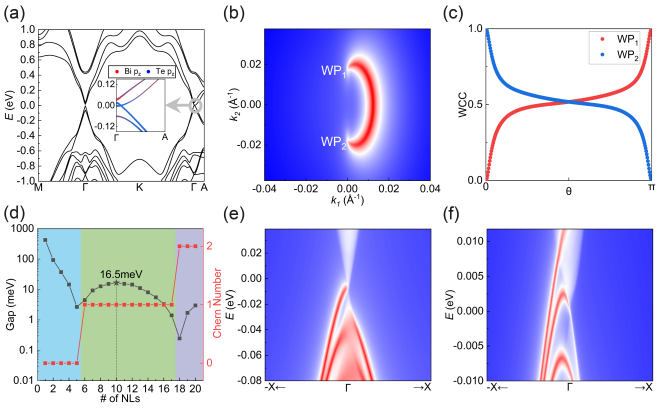

FIG. 14. Topological features of type-III $NiVBi_2Te_5$ in bulk and thin films. (a) Band structure of WSM type-III $NiVBi_2Te_5$. Details of projected band near one of the WPs are shown in the inset. (b) Surface states on the (100) plane, showing a Fermi arc connecting the two WPs. (c) The motions of the sum of WCCs on spheres surrounding each WP in the momentum space. (d) The evolution of band gap and Chern number with thickness of type-III $NiVBi_2Te_5$ slab. Chiral edge states of (e) 6-NL ($\mathcal{C} = 1$) and (f) 20-NL ($\mathcal{C} = 2$) slabs.

[1] M. Z. Hasan and C. L. Kane, Colloquium: Topological insulators, Rev. Mod. Phys. **82**, 3045 (2010).
[2] X.-L. Qi and S.-C. Zhang, Topological insulators and superconductors, Rev. Mod. Phys. **83**, 1057 (2011).
[3] N. P. Armitage, E. J. Mele, and A. Vishwanath, Weyl and Dirac semimetals in three-dimensional solids, Rev. Mod. Phys. **90**, 015001 (2018).
[4] Y. Tokura, K. Yasuda, and A. Tsukazaki, Magnetic topological insulators, Nat. Rev. Phys. **1**, 126 (2019).
[5] A. Sekine and K. Nomura, Axion electrodynamics in topological materials, J. Appl. Phys. **129**, 141101 (2021).
[6] C.-Z. Chang, C.-X. Liu, and A. H. MacDonald, Colloquium: Quantum anomalous Hall effect, Rev. Mod. Phys. **95**, 011002 (2023).
[7] F. D. M. Haldane, Model for a Quantum Hall Effect without Landau Levels: Condensed-Matter realization of the "Parity Anomaly", Phys. Rev. Lett. **61**, 2015 (1988).
[8] R. Yu, W. Zhang, H.-J. Zhang, S.-C. Zhang, X. Dai, and Z. Fang, Quantized Anomalous Hall Effect in Magnetic Topological Insulators, Science **329**, 61 (2010).
[9] C.-Z. Chang, J. Zhang, X. Feng, J. Shen, Z. Zhang, M. Guo, K. Li, Y. Ou, P. Wei, L.-L. Wang, Z.-Q. Ji, Y. Feng, S. Ji, X. Chen, J. Jia, X. Dai, Z. Fang, S.-C. Zhang, K. He, Y. Wang, L. Lu, X.-C. Ma, and Q.-K. Xue, Experimental Observation of the Quantum Anomalous Hall Effect in a Magnetic Topological Insulator, Science **340**, 167 (2013).
[10] M. Mogi, R. Yoshimi, A. Tsukazaki, K. Yasuda, Y. Kozuka, K. S. Takahashi, M. Kawasaki, and

Y. Tokura, Magnetic modulation doping in topological insulators toward higher-temperature quantum anomalous hall effect, Appl. Phys. Lett. **107**, 182401 (2015).

[11] C.-Z. Chang, W. Zhao, D. Y. Kim, H. Zhang, B. A. Assaf, D. Heiman, S.-C. Zhang, C. Liu, M. H. W. Chan, and J. S. Moodera, High-precision realization of robust quantum anomalous Hall state in a hard ferromagnetic topological insulator, Nat. Mater. **14**, 473 (2015).

[12] X.-L. Qi, T. L. Hughes, and S.-C. Zhang, Topological field theory of time-reversal invariant insulators, Phys. Rev. B **78**, 195424 (2008).

[13] R. Li, J. Wang, X.-L. Qi, and S.-C. Zhang, Dynamical axion field in topological magnetic insulators, Nat. Phys. **6**, 284 (2010).

[14] J. Wang, B. Lian, X.-L. Qi, and S.-C. Zhang, Quantized topological magnetoelectric effect of the zero-plateau quantum anomalous Hall state, Phys. Rev. B **92**, 081107(R) (2015).

[15] T. Morimoto, A. Furusaki, and N. Nagaosa, Topological magnetoelectric effects in thin films of topological insulators, Phys. Rev. B **92**, 085113 (2015).

[16] M. Mogi, M. Kawamura, R. Yoshimi, A. Tsukazaki, Y. Kozuka, N. Shirakawa, K. S. Takahashi, M. Kawasaki, and Y. Tokura, A magnetic heterostructure of topological insulators as a candidate for an axion insulator, Nat. Mater. **16**, 516 (2017).

[17] D. Xiao, J. Jiang, J.-H. Shin, W. Wang, F. Wang, Y.-F. Zhao, C. Liu, W. Wu, M. H. W. Chan, N. Samarth, and C.-Z. Chang, Realization of the Axion Insulator State in Quantum Anomalous Hall Sandwich Heterostructures, Phys. Rev. Lett. **120**, 056801 (2018).

[18] X. Wan, A. M. Turner, A. Vishwanath, and S. Y. Savrasov, Topological semimetal and fermi-arc surface states in the electronic structure of pyrochlore iridates, Phys. Rev. B **83**, 205101 (2011).

[19] D. F. Liu, A. J. Liang, E. K. Liu, Q. N. Xu, Y. W. Li, C. Chen, D. Pei, W. J. Shi, S. K. Mo, P. Dudin, T. Kim, C. Cacho, G. Li, Y. Sun, L. X. Yang, Z. K. Liu, S. S. P. Parkin, C. Felser, and Y. L. Chen, Magnetic Weyl semimetal phase in a Kagomé crystal, Science **365**, 1282 (2019).

[20] E. Liu, Y. Sun, N. Kumar, L. Muechler, A. Sun, L. Jiao, S.-Y. Yang, D. Liu, A. Liang, Q. Xu, J. Kroder, V. Süß, H. Borrmann, C. Shekhar, Z. Wang, C. Xi, W. Wang, W. Schnelle, S. Wirth, Y. Chen, S. T. B. Goennenwein, and C. Felser, Giant anomalous Hall effect in a ferromagnetic kagome-lattice semimetal, Nat. Phys. **14**, 1125 (2018).

[21] Y. Xu, Z. Song, Z. Wang, H. Weng, and X. Dai, Higher-Order Topology of the Axion Insulator $EuIn_2As_2$, Phys. Rev. Lett. **122**, 256402 (2019).

[22] Y. Li, J. Li, Y. Li, M. Ye, F. Zheng, Z. Zhang, J. Fu, W. Duan, and Y. Xu, High-Temperature Quantum Anomalous Hall Insulators in Lithium-Decorated Iron-Based Superconductor Materials, Phys. Rev. Lett. **125**, 086401 (2020).

[23] J.-Y. You, Z. Zhang, B. Gu, and G. Su, Two-Dimensional Room-Temperature Ferromagnetic Semiconductors with Quantum Anomalous Hall Effect, Phys. Rev. Applied **12**, 024063 (2019).

[24] Z. Li, Y. Han, and Z. Qiao, Chern Number Tunable Quantum Anomalous Hall Effect in Monolayer Transitional Metal Oxides via Manipulating Magnetization Orientation, Phys. Rev. Lett. **129**, 036801 (2022).

[25] Y. Gong, J. Guo, J. Li, K. Zhu, M. Liao, X. Liu, Q. Zhang, L. Gu, L. Tang, X. Feng, D. Zhang, W. Li, C. Song, L. Wang, P. Yu, X. Chen, Y. Wang, H. Yao, W. Duan, Y. Xu, S.-C. Zhang, X. Ma, Q.-K. Xue, and K. He, Experimental Realization of an Intrinsic Magnetic Topological Insulator, Chin. Phys. Lett. **36**, 076801 (2019).

[26] M. M. Otrokov, I. I. Klimovskikh, H. Bentmann, D. Estyunin, A. Zeugner, Z. S. Aliev, S. Gaß, A. U. B. Wolter, A. V. Koroleva, A. M. Shikin, M. Blanco-Rey, M. Hoffmann, I. P. Rusinov, A. Y. Vyazovskaya, S. V. Eremeev, Y. M. Koroteev, V. M. Kuznetsov, F. Freyse, J. Sánchez-Barriga, I. R. Amiraslanov, M. B. Babanly, N. T. Mamedov, N. A. Abdullayev, V. N. Zverev, A. Alfonsov, V. Kataev, B. Büchner, E. F. Schwier, S. Kumar, A. Kimura, L. Petaccia, G. Di Santo, R. C. Vidal, S. Schatz, K. Kißner, M. Ünzelmann, C. H. Min, S. Moser, T. R. F. Peixoto, F. Reinert, A. Ernst, P. M. Echenique, A. Isaeva, and E. V. Chulkov, Prediction and observation of an antiferromagnetic topological insulator, Nature **576**, 416 (2019).

[27] J. Li, Y. Li, S. Du, Z. Wang, B.-L. Gu, S.-C. Zhang, K. He, W. Duan, and Y. Xu, Intrinsic magnetic topological insulators in van der Waals layered $MnBi_2Te_4$-family materials, Sci. Adv. **5**, eaaw5685 (2019).

[28] J. Li, C. Wang, Z. Zhang, B.-L. Gu, W. Duan, and Y. Xu, Magnetically controllable topological quantum phase transitions in the antiferromagnetic topological insulator $MnBi_2Te_4$, Phys. Rev. B **100**, 121103(R) (2019).

[29] Y. Deng, Y. Yu, M. Z. Shi, Z. Guo, Z. Xu, J. Wang, X. H. Chen, and Y. Zhang, Quantum anomalous Hall effect in intrinsic magnetic topological insulator $MnBi_2Te_4$, Science **367**, 895 (2020).

[30] J. Ge, Y. Liu, J. Li, H. Li, T. Luo, Y. Wu, Y. Xu, and J. Wang, High-Chern-number and high-temperature quantum Hall effect without Landau levels, Natl. Sci. Rev. **7**, 1280 (2020).

[31] M. M. Otrokov, I. P. Rusinov, M. Blanco-Rey, M. Hoffmann, A. Y. Vyazovskaya, S. V. Eremeev, A. Ernst, P. M. Echenique, A. Arnau, and E. V. Chulkov, Unique Thickness-Dependent Properties of the van der Waals Interlayer Antiferromagnet $MnBi_2Te_4$ Films, Phys. Rev. Lett. **122**, 107202 (2019).

[32] D. Zhang, M. Shi, T. Zhu, D. Xing, H. Zhang, and J. Wang, Topological Axion States in the Magnetic Insulator $MnBi_2Te_4$ with the Quantized Magnetoelectric Effect, Phys. Rev. Lett. **122**, 206401 (2019).

[33] C. Liu, Y. Wang, H. Li, Y. Wu, Y. Li, J. Li, K. He, Y. Xu, J. Zhang, and Y. Wang, Robust axion insulator and Chern insulator phases in a two-dimensional antiferromagnetic topological insulator, Nat. Mater. **19**, 522 (2020).

[34] N. D. Mermin and H. Wagner, Absence of Ferromagnetism or Antiferromagnetism in One- or Two-Dimensional Isotropic Heisenberg Models, Phys. Rev. Lett. **17**, 1133 (1966).

[35] F. Huang, M. T. Kief, G. J. Mankey, and R. F. Willis, Magnetism in the few-monolayers limit: A surface magneto-optic Kerr-effect study of the magnetic behavior of ultrathin films of Co, Ni, and Co-Ni alloys on Cu(100) and Cu(111), Phys. Rev. B **49**, 3962 (1994).

[36] J. Zhang, D. Wang, M. Shi, T. Zhu, H. Zhang, and J. Wang, Large Dynamical Axion Field in Topological Antiferromagnetic Insulator $Mn_2Bi_2Te_5$, Chin. Phys.

Lett. **37**, 077304 (2020).

[37] Y. Li, Y. Jiang, J. Zhang, Z. Liu, Z. Yang, and J. Wang, Intrinsic topological phases in $Mn_2Bi_2Te_5$ tuned by the layer magnetization, Phys. Rev. B **102**, 121107(R) (2020).

[38] S. V. Eremeev, M. M. Otrokov, A. Ernst, and E. V. Chulkov, Magnetic ordering and topology in $Mn_2Bi_2Te_5$ and $Mn_2Sb_2Te_5$ van der Waals materials, Phys. Rev. B **105**, 195105 (2022).

[39] L. Cao, S. Han, Y.-Y. Lv, D. Wang, Y.-C. Luo, Y.-Y. Zhang, S.-H. Yao, J. Zhou, Y. B. Chen, H. Zhang, and Y.-F. Chen, Growth and characterization of the dynamical axion insulator candidate $Mn_2Bi_2Te_5$ with intrinsic antiferromagnetism, Phys. Rev. B **104**, 054421 (2021).

[40] H. Zhang, J. Zhang, Y. Zhang, W. Yang, Y. Wang, X. Xu, and F. Liu, A generic dual d-band model for interlayer ferromagnetic coupling in a transition-metal doped $MnBi_2Te_4$ family of materials, Nanoscale **14**, 13689 (2022).

[41] G. Kresse and J. Furthmüller, Efficient iterative schemes for ab initio total-energy calculations using a plane-wave basis set, Phys. Rev. B **54**, 11169 (1996).

[42] J. P. Perdew, K. Burke, and M. Ernzerhof, Generalized Gradient Approximation Made Simple, Phys. Rev. Lett. **77**, 3865 (1996).

[43] A. D. Becke and E. R. Johnson, A simple effective potential for exchange, J. Chem. Phys. **124**, 221101 (2006).

[44] S. Grimme, J. Antony, S. Ehrlich, and H. Krieg, A consistent and accurate ab initio parametrization of density functional dispersion correction (DFT-D) for the 94 elements H-Pu, J. Chem. Phys. **132**, 154104 (2010).

[45] V. Wang, N. Xu, J.-C. Liu, G. Tang, and W.-T. Geng, VASPKIT: A user-friendly interface facilitating high-throughput computing and analysis using VASP code, Comput. Phys. Commun. **267**, 108033 (2021).

[46] A. Togo and I. Tanaka, First principles phonon calculations in materials science, Scr. Mater. **108**, 1 (2015).

[47] K. Momma and F. Izumi, *VESTA3* for three-dimensional visualization of crystal, volumetric and morphology data, J. Appl. Crystallogr. **44**, 1272 (2011).

[48] A. A. Mostofi, J. R. Yates, G. Pizzi, Y.-S. Lee, I. Souza, D. Vanderbilt, and N. Marzari, An updated version of wannier90: A tool for obtaining maximally-localised Wannier functions, Comput. Phys. Commun. **185**, 2309 (2014).

[49] N. Marzari and D. Vanderbilt, Maximally localized generalized Wannier functions for composite energy bands, Phys. Rev. B **56**, 12847 (1997).

[50] I. Souza, N. Marzari, and D. Vanderbilt, Maximally localized Wannier functions for entangled energy bands, Phys. Rev. B **65**, 035109 (2001).

[51] Q. Wu, S. Zhang, H.-F. Song, M. Troyer, and A. A. Soluyanov, Wanniertools: An open-source software package for novel topological materials, Comput. Phys. Commun. **224**, 405 (2018).

[52] S. V. Eremeev, M. M. Otrokov, and E. V. Chulkov, New Universal Type of Interface in the Magnetic Insulator/Topological Insulator Heterostructures, Nano Lett. **18**, 6521 (2018).

[53] T. Hirahara, M. M. Otrokov, T. T. Sasaki, K. Sumida, Y. Tomohiro, S. Kusaka, Y. Okuyama, S. Ichinokura, M. Kobayashi, Y. Takeda, K. Amemiya, T. Shirasawa, S. Ideta, K. Miyamoto, K. Tanaka, S. Kuroda, T. Okuda, K. Hono, S. V. Eremeev, and E. V. Chulkov, Fabrication of a novel magnetic topological heterostructure and temperature evolution of its massive Dirac cone, Nat. Commun. **11**, 4821 (2020).

[54] A. Jain, S. P. Ong, G. Hautier, W. Chen, W. D. Richards, S. Dacek, S. Cholia, D. Gunter, D. Skinner, G. Ceder, and K. A. Persson, Commentary: The Materials Project: A materials genome approach to accelerating materials innovation, APL Mater. **1**, 011002 (2013).

[55] Y. Han, S. Sun, S. Qi, X. Xu, and Z. Qiao, Interlayer ferromagnetism and high-temperature quantum anomalous Hall effect in p-doped $MnBi_2Te_4$ multilayers, Phys. Rev. B **103**, 245403 (2021).

[56] H. Tan, Y. Liu, Z. Wang, and B. Yan, Charge density waves and electronic properties of superconducting kagome metals, Phys. Rev. Lett. **127**, 046401 (2021).

[57] E. Pavarini, E. Koch, F. Anders, and M. Jarrell, *Correlated Electrons: From Models to Materials* (2012).

[58] Z. Li, J. Li, K. He, X. Wan, W. Duan, and Y. Xu, Tunable interlayer magnetism and band topology in van der Waals heterostructures of $MnBi_2Te_4$-family materials, Phys. Rev. B **102**, 081107(R) (2020).

[59] H. Zhang, C.-X. Liu, X.-L. Qi, X. Dai, Z. Fang, and S.-C. Zhang, Topological insulators in Bi_2Se_3, Bi_2Te_3 and Sb_2Te_3 with a single Dirac cone on the surface, Nat. Phys. **5**, 438 (2009).

[60] C.-X. Liu, X.-L. Qi, H.-J. Zhang, X. Dai, Z. Fang, and S.-C. Zhang, Model hamiltonian for topological insulators, Phys. Rev. B **82**, 045122 (2010).

[61] H. Wang, D. Wang, Z. Yang, M. Shi, J. Ruan, D. Xing, J. Wang, and H. Zhang, Dynamical axion state with hidden pseudospin Chern numbers in $MnBi_2Te_4$-based heterostructures, Phys. Rev. B **101**, 081109(R) (2020).

[62] G. Xu, H. Weng, Z. Wang, X. Dai, and Z. Fang, Chern Semimetal and the Quantized Anomalous Hall Effect in $HgCr_2Se_4$, Phys. Rev. Lett. **107**, 186806 (2011).

[63] A. A. Burkov and L. Balents, Weyl Semimetal in a Topological Insulator Multilayer, Phys. Rev. Lett. **107**, 127205 (2011).

[64] A. A. Zyuzin, S. Wu, and A. A. Burkov, Weyl semimetal with broken time reversal and inversion symmetries, Phys. Rev. B **85**, 165110 (2012).